



OPEN

Nanocrystalline ZnON; High mobility and low band gap semiconductor material for high performance switch transistor and image sensor application

Eunha Lee¹, Anass Benayad¹, Taeho Shin¹, HyungIk Lee¹, Dong-Su Ko¹, Tae Sang Kim², Kyoung Seok Son², Myungkwan Ryu², Sanghun Jeon³ & Gyeong-Su Park¹

¹Analytical Science Group, Samsung Advanced Institute of Technology, Samsung Electronics Corporations, Yongin-Si, Gyeonggi-Do, 446-712, Korea, ²Display Lab, Samsung Advanced Institute of Technology, Samsung Electronics Corporations, Yongin-Si, Gyeonggi-Do, 446-712, Korea, ³Department of Applied Physics, Korea University, Sejongro Sejong, 339-700, Korea.

Received
5 March 2014

Accepted
22 April 2014

Published
13 May 2014

SUBJECT AREAS:
ELECTRONIC DEVICES
SEMICONDUCTORS
ELECTRONIC PROPERTIES AND
MATERIALS

Correspondence and requests for materials should be addressed to E.L. (eunhayo.lee@samsung.com) or S.J. (jeonsh@korea.ac.kr)

Interest in oxide semiconductors stems from benefits, primarily their ease of process, relatively high mobility (0.3–10 cm²/vs), and wide-bandgap. However, for practical future electronic devices, the channel mobility should be further increased over 50 cm²/vs and wide-bandgap is not suitable for photo/image sensor applications. The incorporation of nitrogen into ZnO semiconductor can be tailored to increase channel mobility, enhance the optical absorption for whole visible light and form uniform micro-structure, satisfying the desirable attributes essential for high performance transistor and visible light photo-sensors on large area platform. Here, we present electronic, optical and microstructural properties of ZnON, a composite of Zn₃N₂ and ZnO. Well-optimized ZnON material presents high mobility exceeding 100 cm²V⁻¹s⁻¹, the band-gap of 1.3 eV and nanocrystalline structure with multiphase. We found that mobility, microstructure, electronic structure, band-gap and trap properties of ZnON are varied with nitrogen concentration in ZnO. Accordingly, the performance of ZnON-based device can be adjustable to meet the requisite of both switch device and image-sensor potentials. These results demonstrate how device and material attributes of ZnON can be optimized for new device strategies in display technology and we expect the ZnON will be applicable to a wide range of imaging/display devices.

Recently, zinc oxide (ZnO)-based thin-film transistors (TFTs), in which the active semiconductor materials possess a high mobility of around $\sim 3 \text{ cm}^2 \text{ V}^{-1} \text{ s}^{-1}$ as well as an ultraviolet (UV)-visible bandgap of 3.2–3.5 eV, have been extensively investigated for their potential in the construction of large-area displays and photosensors^{1–7}. From the perspective of device fabrication, their advantages include compatibility with the existing process technology, low-temperature processability, and optical transparency^{8–9}. Furthermore, their exceptional electrical characteristics such as high on/off ratio, transconductance, switching speed, and stability under electrical and optical stresses provide the motivation for use in the manufacture of real display technologies^{10–11}. Specifically, amorphous oxide semiconductors offer a negligible threshold voltage variation over the entire wafer while maintaining high field effect mobility characteristics, allowing its application in memory¹², high density logic¹³, and high power devices¹⁴. However, for realizing ultra-definition, 3D, and other promising display technologies in the future, the mobility of active oxide channel materials need to be further increased over 30 cm² V⁻¹ s⁻¹¹⁵. Also, considering the fact that the most promising solution for obtaining large-area interactive displays is the photosensing process, which has the potential to remove RC delay issues, the photosensors should possess high-speed responsivity^{16–17}. In addition, owing to the technological need for a wide range of visible light-wavelength selectivity, the bandgap of active oxide semiconductors should be reduced to less than 1.6 eV, allowing the absorption of the entire visible light spectrum¹⁷. However, oxide semiconductors have a relatively large bandgap in the range 2.9–3.5 eV. Furthermore, amorphous oxide semiconductors have one critical weakness, namely persistent photo-conductivity, which leads to a light-induced threshold voltage instability¹⁸. In order to resolve these issues, various materials and approaches have been introduced and studied over the past few years.

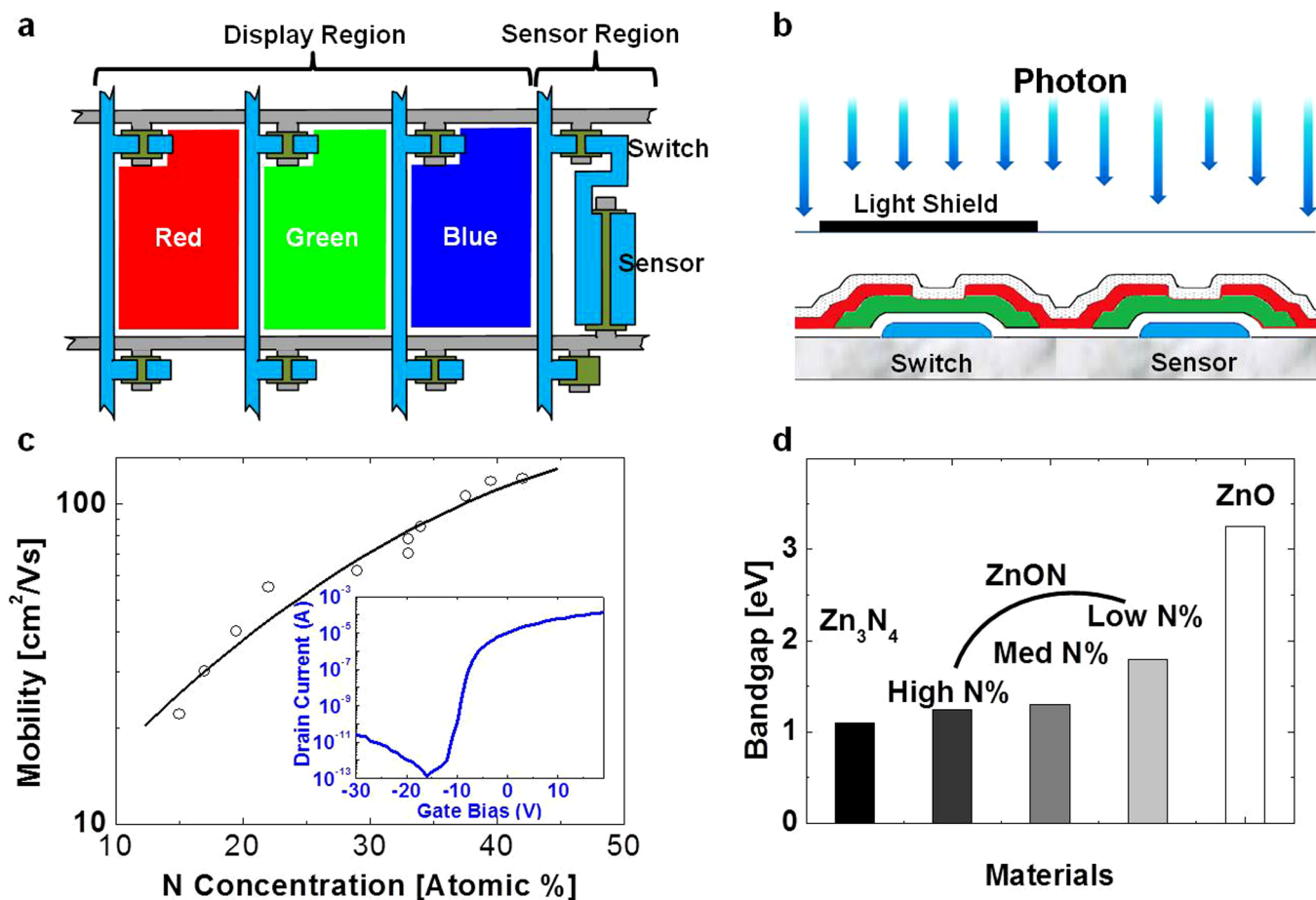


Figure 1 | Pixel structure comprising of display and sensor parts in which ZnO and ZnON active semiconductor present tunable electrical and optical properties with nitrogen concentration in film. (a) The schematic of pixel structure composed of display and sensor regions where core devices are formed of transistors as for switch and sensor. (b) Cross-sectional view of photo-sensor region comprised of switch and sensor which should present different responsivity to the light (c) The evolution of Hall mobility characteristics of ZnON with N concentration in film. The inset shows the representative transfer curve characteristic of ZnON TFT (d) The band-gap of various materials, Zn₃N₄, ZnON with different N concentration, and ZnO, which were extracted by visible-IR spectrometer analysis.

Zinc oxynitride (ZnON) is a composite of ZnO, ZnO_xN_y and Zn₃N₂, the latter being a II–V semiconductor with an antiscandium structure with great potential for optoelectronic applications. ZnON possesses a high mobility ($\sim 100 \text{ cm}^2 \text{ V}^{-1} \text{ s}^{-1}$) and a wide bandgap range of 1.01–2.11 eV^{19–20}. Since generally the reaction of Zn with O occurs during the growth of ZnON, careful adjustment of the O₂ to N₂ gas ratio in the reactive sputtering chamber leads to the formation of amorphous or highly disordered ZnON. It is observed that ZnON with N/(O + N) of more than 86% has a small bandgap of 1.3 eV and its intrinsic mobility exceeds $100 \text{ cm}^2 \text{ V}^{-1} \text{ s}^{-1}$. Such a low bandgap ZnON semiconductor material enables the photosensor to have wide wavelength selectivity, leading to responsivity to all visible light, in contrast to ZnO, which has a bandgap of 3.3 eV and is confined to the UV spectrum. Also, the high mobility of ZnON leads to the production of high-speed switching devices, resulting in the realization of high-motion-speed displays²⁰. Therefore, ZnON material has the potential to overcome the performance issues of amorphous oxide semiconductors and realize high speed interactive displays. However, in-depth and systematic analyses on ZnON comprising different amounts of nitrogen have not yet been carried out.

In this report, the interactive display system with both display and sensor functionalities is first proposed. Then, a sensor containing switch and photo-sensor elements, both of whose active semiconductor layer is the ZnON semiconductor, is examined and the main reason for the need for the active semiconductor material to

possess high mobility and low bandgap is discussed. Hall mobility, bandgap, microstructure, electronic structure, and trap properties of ZnON are explored in order to understand future application of ZnON in interactive display technology. Bright field transmission electron microscope and selected area electron diffraction patterns confirmed the presence of nanostructures in all ZnO and ZnON samples. Additionally, a two-dimensional map from UV-visible and near-infrared (IR) transient absorption analysis of ZnON exhibits the multi-bandgap structure resulting from the contributions of nanosized ZnO, and Zn₃N₂ particles in amorphous ZnO_xN_y matrix in various ratios and of varying sizes. Finally, the trap analysis of ZnON clarifies the high mobility characteristics of ZnON. This study provides a material design strategy for ZnON suitable for high-performance displays and photonic devices.

Results

In comparison to a one-way information delivery display, an interactive display operates both display and sensor at the same time²¹. It needs to detect the presence of touch or photo-signal in order to receive the input information from a user^{17,22}. Figure 1a shows the simplified pixel structure of an interactive display comprised of the display and sensor sections. In the display region, in order to address each pixel and control the light brightness, a switch component usually formed from a bottom-gated thin-film transistor (TFT) is employed in every sub-pixel. Here, the active semiconductor is the



key material in determining the driving speed. More specifically, high mobility of the channel material enables the realization of ultra-definition and large-area displays with 3D visual effects²⁰. On the other hand, the sensor should be responsive to light in order to play a role in ensuring remote touch functionality for large-area interactive displays²². Also, similar to the display section, a switch should be used and connected to the sensor. Considering the process compatibility, the sensor element needs to contain the same active semiconductor and the same device architecture such as the bottom gate TFT structure seen in Figure 1b.

TFTs with ZnON active semiconductor deposited by reactive radio frequency (RF) magnetron sputtering using a Zn target and Ar/O₂/N₂ mixture gas were fabricated. The details are presented in the Methods section and the Hall mobilities of ZnON with respective nitrogen contents (N/(Zn + O + N)) are presented in Figure 1c. The representative transfer curve of a ZnON TFT with a gate length of 10 μm and a gate width of 20 μm is presented in the inset. The saturation mobility is 45.8 cm² V⁻¹ s⁻¹, which agrees approximately with the Hall mobility of ZnON films (~50 cm² V⁻¹ s⁻¹). In order to examine the influence of nitrogen concentration on the optical bandgap of ZnON, UV-visible spectrometer analysis was performed. As seen in Figure 1d, the bandgaps of Zn₃N₂ and ZnO materials are found to be 1.1 and 3.25 eV, respectively. The bandgaps of ZnO_{0.73}N_{0.27}, ZnO_{0.51}N_{0.49}, and ZnO_{0.14}N_{0.86}, mixtures of Zn₃N₂ and ZnO, are 1.8, 1.5, and 1.3 eV, respectively. The overall composition of the ZnON thin films with different nitrogen and oxygen content is measured by Rutherford Backscattering Spectrometry (RBS) analysis, where atomic concentrations of oxygen and nitrogen in ZnON film can be absolutely quantified. Hereafter, ZnO_{0.73}N_{0.27}, ZnO_{0.51}N_{0.49}, and ZnO_{0.14}N_{0.86} are referred to as ZnON (Low N%), ZnON (Med N%), and ZnON (High N%), respectively.

Based on the Hall mobility and bandgap measurements, it is supposed that there are strong correlations between ZnON nitrogen content and its material and electrical properties. The structure and composition of ZnON thin films are controlled by controlling the oxygen and nitrogen flow rates during the reactive sputtering process. A large ratio of nitrogen to oxygen flow rate results in the substantial substitution of oxygen with nitrogen in ZnO, thereby forming ZnON films. In addition to the compositional variation, the crystallinity of ZnON strongly depends on the oxygen flow rate, as shown in the synchrotron X-ray diffraction (XRD) patterns in Figure 2a. The XRD peaks for ZnO and ZnON (Low N%) indicate that both samples have crystalline structures. The (002) Bragg diffraction patterns of the hexagonal ZnO structure is dominant in the

XRD data. As nitrogen content is increased, this sharp peak disappears and only the broad peaks remain. Wide-angle XRD patterns for all samples show a broad peak, a typical feature of amorphous or nanocrystalline structures, implying that all samples have the amorphous or nanocrystalline matrix. In order to probe the structure of the matrix in greater detail, transmission electron microscopy (TEM) was performed. The bright-field (BF) TEM images, shown in Figures 2b–2d, demonstrate that all the samples contain a crystallized part. The contrast variations (labeled using dark and light gray colors) observed in the BF TEM images verifies the crystallization of the thin films; the crystalline areas orientated along a zone axis appear with a dark contrast (Bragg diffraction). The insets depicting selected-area electron diffraction patterns (SADPs) of the ZnON and ZnO thin films confirm partial or full crystallization of the samples. The SADP obtained from the ZnON (High N%) sample (the inset of Figure 2b) reveals a mixed microstructure of amorphous and crystalline phases. As the nitrogen content of ZnON thin films increases, the typical columnar microstructure of ZnO tends to be oriented randomly and the thin films include amorphous phases.

To elucidate the microstructure and the chemical binding states of a ZnON thin film, a detailed study of the ZnON (High N%) thin films was carried out as shown in Figure 3. The high resolution TEM analyses of Figure 3a show that the microstructure of ZnON contains a few nanometer-sized crystallites. Its Fourier diffractogram (Figure 3b) indicates that these nanosized crystallites are combined with an amorphous phase. The two nano-beam electron diffraction (NBD) patterns presented in Figures 3c and 3d corroborate the complex microstructure of the nanometer-sized mixed phases. Since these were obtained with an electron probe of ~5 nm size in a micro-probe STEM mode, the NBD patterns consisting of diffused rings and diffracted spots with several crystalline orientations provide knowledge of the approximate size of the crystalline grain and the crystallinity of the component phases.

To clarify the local electronic structure of ZnON, XPS analysis of the Zn 2*p*, O 1*s*, and N 1*s* core levels was performed with Ar ion-beam etching process. The O 1*s* (529.6 eV) and Zn 2*p*_{3/2} (1020.8 eV) core peaks are assigned to O²⁻ ions and Zn²⁺ cations binding energies, typically observed in ZnO materials. The N 1*s* core peak (395.5 eV) observed after the Ar ion-beam etching process is attributed to the nitrogen surrounded by Zn atoms, generally found in Zn₃N₂. Besides the Zn 2*p*_{3/2} core peak usually studied to understand the chemical states, analysis of the Zn L₃M₄₅M₄₅ Auger peaks provides detailed information about the strong chemical effect observed from the shapes, intensities, and locations of the Auger

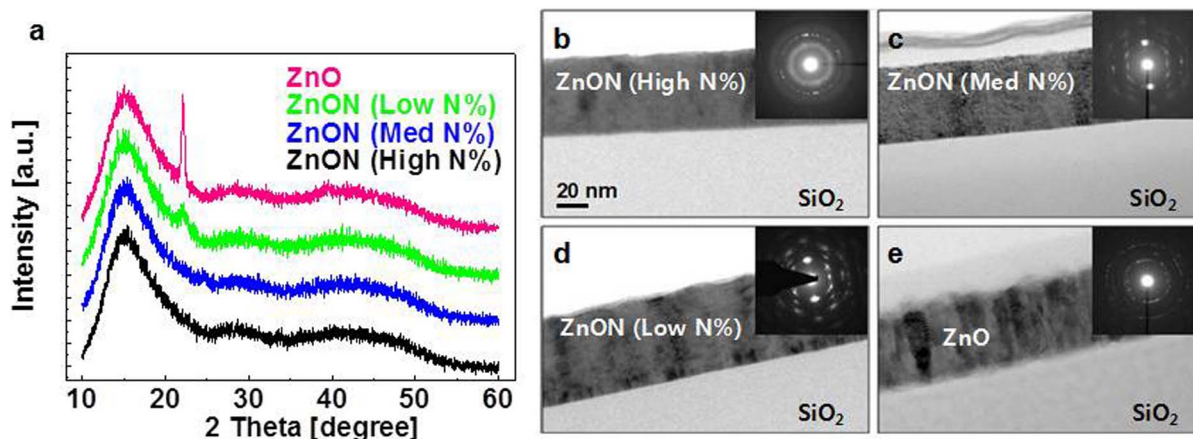


Figure 2 | Crystallinity and microstructure of ZnO and ZnON thin films with different nitrogen contents. (a) Synchrotron X-ray diffraction (XRD) patterns present that both pure ZnO and ZnON (Low N%) are crystallized. The peaks appeared in ZnO and ZnON (Low N%) samples correspond to the ZnO (002) diffraction peak. (b) ~ (e) Bright-field transmission electron microscope (TEM) images show all the samples contain crystallized portion, even in ZnON (High N%). The insets in right top depicts the selected-area electron diffraction patterns (SADPs) confirming partial or full crystalline pattern in all the ZnO and ZnON samples.

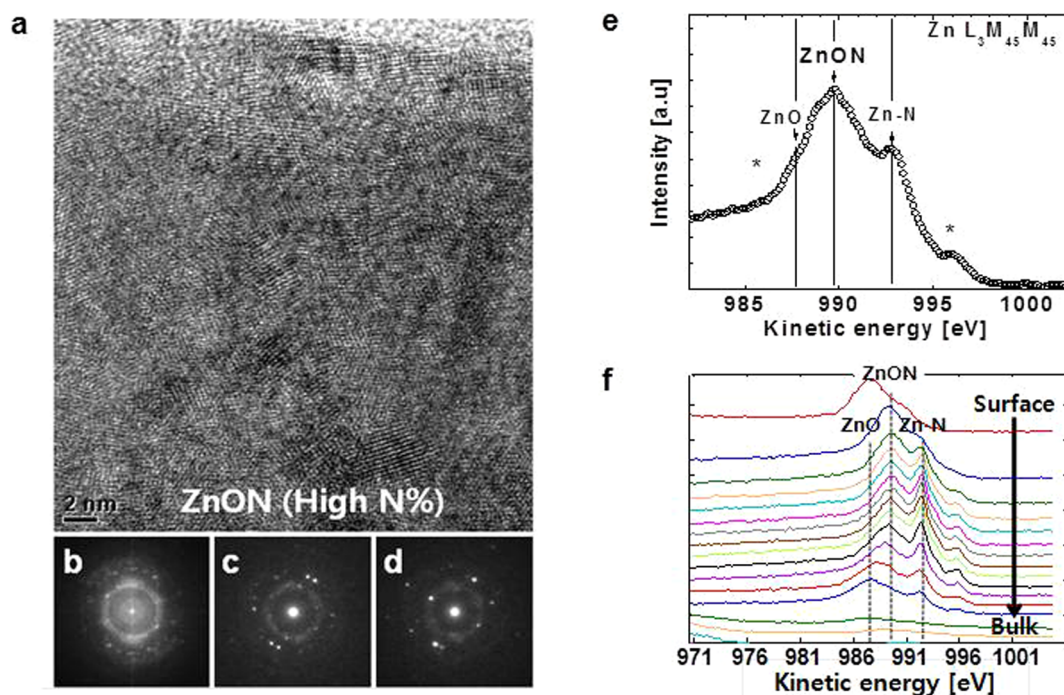


Figure 3 | Microstructure and chemical bonding states of the ZnON (High N%) sample. (a) High resolution transmission electron microscope (HRTEM) image showing randomly oriented and dispersed nano-sized (~5 nm) grains, (b) diffractogram of HRTEM (a), (c) and (d) nano-beam electron diffraction (NBD) patterns acquired with ~5 nm probe size, (e) X-ray photoelectron spectroscopy (XPS) showing Auger transition of Zn atom (f) XPS depth profiling indicates the formation of ZnO phase at the surface of the ZnON thin film.

lines involving deep Zn $2p_{3/2}$ (L_3), and shallow Zn $3d_{5/2-3/2}$ (M_{45}) core levels. The Auger line shown in Figure 3e arises from three nearly degenerate levels 1D , 3P , and 1G , and two extreme levels 1S and 3F constituting the higher and lower energy shoulders of the Auger line (labeled by stars in Figure 3e)²³. As a first approximation the main peak of each chemical group can be represented by the 1D , 3P , and 1G triad (nX) symbolized by a dashed line in Figure 3e and assigned to the ZnN, ZnON, and ZnO species respectively. The Auger line depth profile (Figure 3f) shows high ZnO concentration at the surface and multiple phases ZnN, ZnON, and ZnO in the bulk. This result corroborates the coexistence of multiple diffraction spots and rings characterizing a mixture of amorphous ZnON and nanocrystalline ZnO and ZnN phases. The effect of the multiphase composition on the electronic and bandgap structures is discussed based on the results of transient electrical and optical spectroscopy.

Instead of a conventional optical absorption technique, changes in the bandgap structure with compositional variation of the ZnON films was examined using femtosecond transient absorption (TA) measurements. The conventional technique, which involves measuring optical absorption coefficient with the Tauc method, has been employed for examining a variety of semiconducting materials. However, in the case of a multiphase material with multiple bandgap values, this typical method does not conclusively distinguish between the different bandgaps. That is why femtosecond TA measurements were performed, whose results can be seen in Figure 4. The details of the experiment are presented in the Methods section. The transient absorption technique uses a pair of laser pulses: pump pulse for excitation and probe pulse for measuring absorption. Once the pump pulse excites electrons from the valence band to the conduction band (see Figure 4a (i)), the excited hot carriers relax to the band edges via electron-phonon interaction typically within several picoseconds (intra-band relaxation, Figure 4a (ii)) and continue to relax back to the original ground state via electron-hole recombination (inter-band relaxation). Since the inter-band relaxation takes place much more slowly than the intra-band relaxation, the carriers stay populated at the band edges for a certain time period until the

inter-band relaxation is complete. If the absorption spectrum is measured at this moment, transient absorption is seen to decrease selectively only at the wavelengths corresponding to the bandgap because of fewer electrons being available for absorption at the band edge as shown in Figure 4a (iii). If there are multiple inter-band transitions involved, this scheme yields the corresponding multiple transient absorption peaks. Therefore, the transient absorption measurement reveals not only carrier dynamics but also band structures in a more straightforward way than a conventional optical absorption technique, which may not decisively differentiate between multiple inter-band transitions owing to the overlap of absorption peaks^{24–25}.

Figure 4b shows the experimental results of transient absorption study on the ZnON samples. Transient absorption spectra as a function of delay times are illustrated as a two-dimensional representation in which x and y axes indicate wavelengths and delay times, respectively. For all the samples, hot carriers relax to the band edges on the sub-picosecond timescale and undergo a further inter-band relaxation to the ground state in several tens of picoseconds. As mentioned earlier, on account of the different timescales for intra- and inter-band relaxations, band-edge transitions are clearly observed at small delay times. The transient absorption spectra of the ZnO sample (see the bottom of Figure 4b) show a very sharp absorption band at 3.4 eV, indicating that ZnO has a well-defined band structure with bandgap energy of 3.4 eV. As nitrogen content is increased within ZnON, however, the position of the absorption band shifts to a higher wavelength, which implies decreasing bandgap values. For ZnON (Low N%), two absorption bands are clearly observed. This suggests that two major phases coexist in the ZnON film. One is definitely an oxygen-rich ZnON phase whose band gap is close to that of the original ZnO phase. Its broader bandwidth is possibly due to chemical inhomogeneity in the presence of a small amount of nitrogen. The other newly emerged absorption band at 2.4 eV indicates another nitrogen-rich ZnON phase. With increasing N content in ZnON, the absorption peak shifts to higher wavelengths, indicating that the band gap becomes smaller as nitrogen increases. For ZnON (High N%), the absorption band is decreased to 1.3 eV.

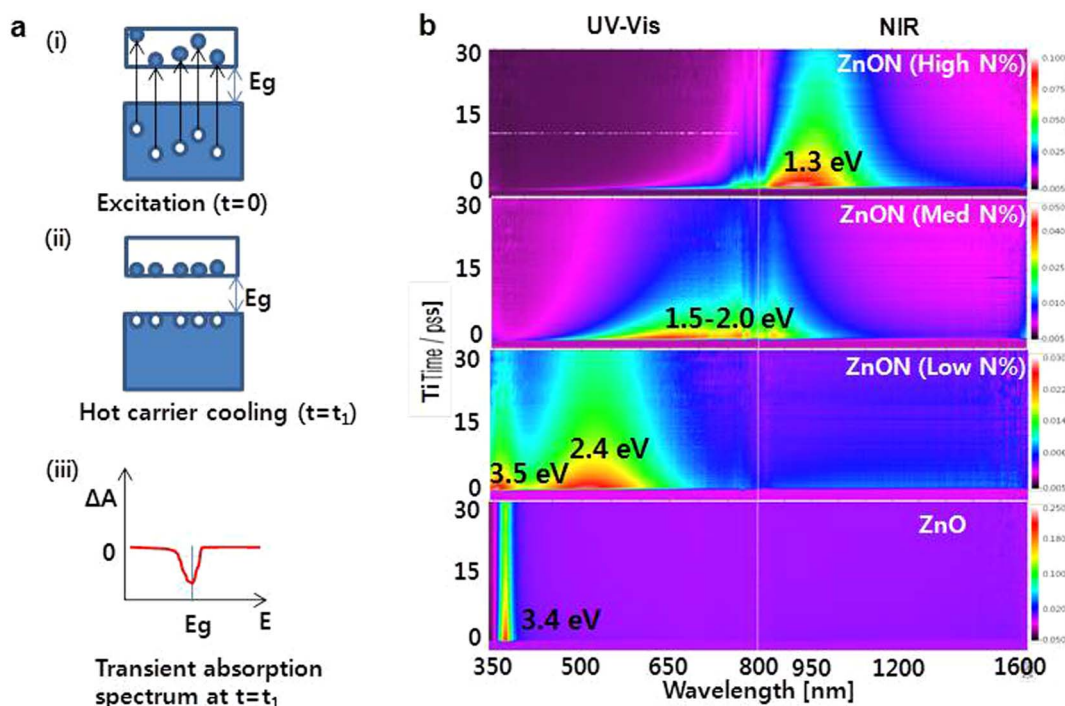


Figure 4 | Femtosecond transient absorption measurement results (a) Schematic for a band gap identification using ultrafast carrier dynamics. (b) 2D representation of UV-Vis and NIR transient absorption spectra. The UV-Vis (330–850 nm) and NIR (750–1600 nm) absorption experiments were carried out separately and then their spectra were merged together. The color scale represents change in transmission ($\Delta T/T$). The absorption peaks shift towards longer wavelengths with increasing nitrogen density indicating that the band gap becomes smaller at higher nitrogen density.

The bandgap narrowing is explained by the occupation of the nitrogen $2p$ band. The nitrogen $2p$ band located above the oxygen $2p$ band becomes occupied due to the high N content and accordingly the valence band maximum is elevated. On the other hand, the conduction band minimum determined by the Zn $4s$ band is not influenced by the addition of nitrogen. However, due to the combined effect of the shift in valence band maximum and conduction band minimum, the band gap becomes narrower. Accordingly, the photoresponsive characteristic of ZnON is changed as seen in Supporting Information.

In addition to the band shift, the absorption band becomes noticeably broader with increasing nitrogen content. The broad band in ZnON is attributed to the spectral overlap of multiple phases with different chemical bonding states and stoichiometry (inhomogeneous broadening) as evidenced by the XPS results. The inhomogeneity arises naturally from the difference in the number of valence electrons between oxygen and nitrogen atoms. In other words, while pure ZnO and Zn_3N_2 are supported by their own crystal structures, no unique crystal structure for ZnON exist, thereby producing diverse ZnON complexes with locally different stoichiometry.

The final stage in the construction of an accurate band structure is defect characterization, which allows us to determine the defect levels in the energy gap and probe the origin of each defect. Among several defect analysis techniques, photo-induced current transient spectroscopy (PICTS) is an appropriate method to measure defects in ZnO and ZnON samples. The PICTS method measures temperature-dependent transient photocurrent due to thermal emission of trapped charge carriers generated by light pulse excitation. The defect energy level and its concentration are then analyzed from this transient photocurrent. Since the charge carriers trapped in defects can be emitted by thermal excitation with an emission rate e_n , as shown in the following equation, the activation energy (E_d) of each defect can be determined by the slope of an Arrhenius plot of $\ln(e_n/T^2)$ versus $1/T$. The defect concentration is also calculated using the value of the peak amplitude in the spectrum. The schematic of the

experimental set up is presented in Figure 5a and the details are presented in the Methods section. Figure 5b shows the PICTS spectra of ZnON. Two major peaks at ~ 90 K and ~ 300 K are observed. Activation energies are determined by Arrhenius plots as shown in Fig. 5c. The defects found at ~ 90 K have an activation energy of ~ 0.2 eV and a trap concentration of $\sim 10^{16}/\text{cm}^3$. The origin of this defect is related to nitrogen. Generally, deep-level transient spectroscopy (DLTS) measurement of a ZnO single crystal indicates an activation energy of ~ 0.3 eV and a trap concentration of $\sim 10^{15}/\text{cm}^3$ ²⁶. However, for ZnON materials, the number of defects located in the shallow energy level [0.2–0.5 eV] is increased by $\sim 10^{16}/\text{cm}^3$. Interestingly, the shallow energy defect of ZnON is decreased with increasing nitrogen content in ZnON. Quantitatively, the number of defects in the shallow energy level of ZnON (High N%), ZnON (Med N%), and ZnON (Low N%) are 1.72×10^{16} , 2.04×10^{16} and $3.08 \times 10^{16}/\text{cm}^3$, respectively. In a previous report, high Hall mobility and field effect mobility for ZnON were explained considering only the effect of low effective mass of Zn_3N_2 . However, taking into account the fact that the tailing state defect is the critical ingredient in influencing mobility, it can be inferred that the tailing state with nitrogen content in ZnON is another contributing element in the determination of the mobility of ZnON.

Discussion

High resolution, superior motion speed, and large-area displays with remote touch functionality are in great demand to provide interactive information transfer instead of the conventional one-way method. To this end, the displays must integrate photo-sensors with switching transistors to detect the external input visible light signal. To provide the desirable attributes essential for both devices, the active semiconductor materials should possess high mobility, low bandgap, and uniform microstructure. In this investigation, the electronic, optical, and structural properties of ZnON, a composite of Zn_3N_2 and ZnO prepared by modulating the ratio of nitrogen to oxygen in ZnO, are studied. Extensive analysis of ZnON indicates

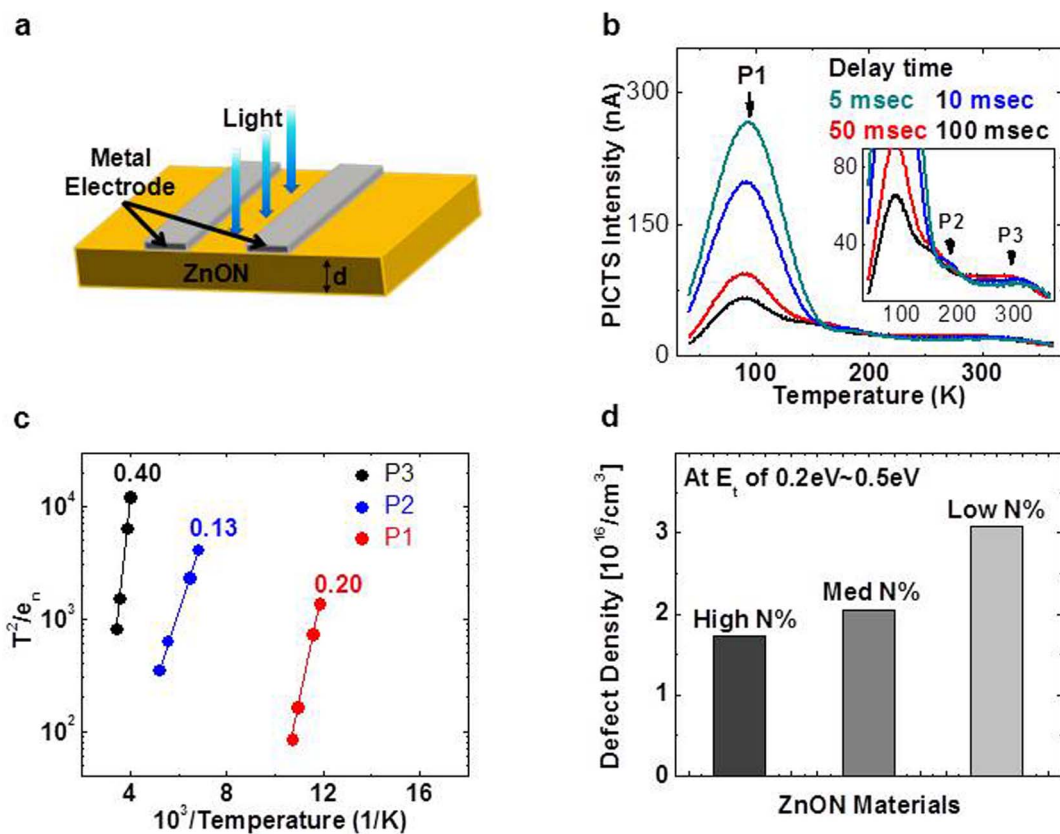


Figure 5 | Defect analysis by photo-induced current transient spectroscopy (PICTS) (a) Schematic of experimental setup. (b) PICTS spectra of ZnON, where two major peaks are observed at 90 K and 300 K. (c) Arrhenius plots for three peaks. (d) The number of defect located at 0.2 eV–0.5 eV versus various ZnON materials.

that mobility, microstructure, electronic structure, bandgap, and trap properties of ZnON vary with the nitrogen content in ZnO. Accordingly, the performance of ZnON-based devices can be adjusted to meet the requirements of both the photo-sensor and the switching devices. These results demonstrate how the device and material attributes of ZnON can be optimized for new device strategies in display technology. Furthermore, we expect the ZnON to be applicable in a wide range of imaging/display devices and systems.

Methods

Zn_xO_yN_z thin films were deposited by reactive radio-frequency (rf) magnetron sputtering using zinc (99.995% purity) target under controlled Ar (99.99% purity), O₂ (99.999% purity) and N₂ (99.999% purity) mixed plasma. 50 nm thick films were deposited on SiO₂/Si wafer and amorphous glass substrate at 50 °C. The Zn_xO_yN_z stoichiometry was controlled by adjusting the partial pressure inside the sputtering chamber. In order to control the oxygen content in the films, the O₂ partial pressure (3.6–28.1 mPa) in the chamber was varied during the deposition by adjusting the O₂ flow rate (1–6 sccm) and the total gas pressure (0.4–0.8 Pa), while the rf power (300 Watt), the N₂ (100 sccm) and Ar flow rates (10 sccm) were kept constant. ZnON with nitrogen content of 36.7, 22.7, and 12.7% were deposited in order to study the electronic, optical and structural variation depending on nitrogen amount in ZnON; Zn₃N₂, and ZnO thin films were deposited as well for reference. The device fabrication is found elsewhere²⁰.

The microstructure and the crystal structure of ZnON thin films were examined by a TEM (FEI Titan 80–300) operated at 300 keV. High Resolution Transmission Electron Microscopy (HR-TEM) and Nano-Beam electron Diffraction in STEM mode were carried out. High-Angle annular Dark-Field (HAADF) in Scanning Transmission Electron Microscopy (STEM) mode was used to determine the compositional distribution of nano-structure.

The electronic structure of ZnON films was carried out by XPS analyses performed with ULVAC-Φ Versa Probe spectrometer using a focused (diameter of the irradiated area = 100 μm) mono-chromatized Al K_α radiation (1486.6 eV). Depth profile analysis was performed by a sequenced Ar⁺ ions sputtering from surface to substrate with 1 KeV beam energy within 2 min sputtering step.

Transient absorption experiments were conducted using a Ti-sapphire regenerative amplifier which produces 1 kHz pulses with a temporal duration of 60 fs at a center wavelength of 800 nm. Combined with an optical parametric amplifier and subsequent nonlinear doubling or mixing crystals if necessary, the system offers broad wavelength tunability from 240 to 2600 nm for pump pulses. For the present study, the pump wavelength was set to 360 nm. Two separate white light super-continuum sources were generated as probe pulses for UV-VIS or NIR absorption measurements. After being transmitted through samples, the intensity of the super-continuum radiation was recorded by either UV-VIS (330–850 nm) or NIR (750–1600 nm) spectrometer as a function of pump-probe delay times.

Defect levels and densities were analyzed by PICTS measurements. Metallic Ohmic electrodes were deposited by thermal evaporation of metal Al on ZnON thin films because it is known that the sample requires ohmic contacts for better PICTS measurement. Then light pulses of 472 nm (blue LED) were used to excite carrier as shown in Figure 5(a). PICTS measurements were performed with rate windows ranging from 21.4 ms to 430 ms using Sula Technologies DLTS instrument. ZnON sample was measured under bias voltage of 4 V and in the temperature range of 40 K ~ 360 K.

- Dehuff, N. L. *et al.* Transparent thin-film transistors with zinc indium oxide channel layer. *J. Appl. Phys.* **97**, 064505 (2005).
- Hu, L. *et al.* An Optimized Ultraviolet-A Light Photodetector with Wide-Range Photoresponse Based on ZnS/ZnO Biaxial Nanobelt. *Advanced Materials* **24**, 2305 (2012).
- Xu, C., Wu, J., Desai, U. V. & Gao, D. High-efficiency solid-state dye-sensitized solar cells based on TiO₂-coated ZnO nanowire arrays. *Nano Letters* **12**, 2420 (2012).
- Hsieh, H. H. & Wu, C. C. Amorphous ZnO transparent thin-film transistors fabricated by fully lithographic and etching processes. *Appl. Phys. Lett.* **91**, 013502 (2007).
- Bera, A. & Basak, D. Role of defects in the anomalous photoconductivity in ZnO nanowires. *Appl. Phys. Lett.* **94**, 163119 (2009).
- Liu, P. T., Chou, Y. T., Teng, L. F. & Fuh, C. S. High-gain complementary inverter with InGaZnO/pentacene hybrid ambipolar thin film transistors. *Appl. Phys. Lett.* **97**, 083505 (2010).
- Jeon, S. *et al.* Gated three-terminal device architecture to eliminate persistent photoconductivity in oxide semiconductor photosensor arrays. *Nature Materials* **11**, 301 (2012).



8. Seo, D. *et al.* Fully transparent InGaZnO thin film transistors using indium tin oxide/graphene multilayer as source/drain electrodes. *Appl. Phys. Lett.* **97**, 172106 (2010).
9. Jeon, S. *et al.* Nanometer-Scale Oxide Thin Film Transistor with Potential for High-Density Image Sensor Applications. *ACS Applied Materials and Interfaces* **3**, 1 (2010).
10. Ghaffarzadeh, K. *et al.* Instability in threshold voltage and subthreshold behavior in Hf–In–Zn–O thin film transistors induced by bias-and light-stress. *Appl. Phys. Lett.* **97**, 113504 (2012).
11. Ghaffarzadeh, K. *et al.* Persistent photoconductivity in Hf–In–Zn–O thin film transistors. *Appl. Phys. Lett.* **97**, 143510 (2012).
12. Kim, H. *et al.* Three-Dimensional Integration Approach to High-Density Memory Device. *IEEE Trans. Elect. Dev.* **58**, 3820 (2011).
13. Lee, M.-J. *et al.* Low-Temperature-Grown Transition Metal Oxide Based Storage Materials and Oxide Transistors for High-Density Non-volatile Memory. *Advanced Functional Materials* **19**, 1587 (2009).
14. Jeon, S. *et al.* High Performance Bilayer Oxide Transistor for Gate Driver Circuitry Implemented on Power Electronic Device. *VLSI Technology Symposium Digest of Technical Papers* 125 (2012).
15. Choi, H., Jeon, S. *et al.* Thickness dependent low-frequency noise characteristics of a-InZnO thin film transistors under light illumination. *Appl. Phys. Lett.* **104**, 023505 (2014).
16. Choi, H., Jeon, S. *et al.* Field-induced macroscopic barrier model for persistent photoconductivity in nanocrystalline oxide thin-film transistors. *Appl. Phys. Lett.* **104**, 133507 (2014).
17. Ahn, S. *et al.* Metal Oxide Thin Film Photo-Transistor for Remote Touch Interactive Display. *Advanced Materials* **24**, 2631 (2012).
18. Janotti, A. & Van de Walle, C. G. Native point defects in ZnO. *Phys. Rev. B* **76**, 165202 (2007).
19. Kim, H. *et al.* Anion control as a strategy to achieve high-mobility and high-stability oxide thin-film transistors. *Scientific Reports* **3**, 1459 (2013).
20. Ye, Y., Lim, R. & White, J. M. High mobility amorphous zinc oxynitride semiconductor material for thin film transistors. *J. Appl. Phys.* **106**, 074512 (2009).
21. Park, S. *et al.* Effects of operational and geometrical conditions upon photosensitivity of amorphous InZnO thin film transistors. *J. Vacuum Science and Technology B*, **31**, 050605-1 (2013).
22. Ahn, S. *et al.* High Performance Nanowire Oxide Photo-Thin Film Transistors. *Advanced Materials* **25**, 5549 (2011).
23. Kowalczyk, S. P. *et al.* X-Ray Photoemission from Zinc: Evidence for Extra-Atomic Relaxation via Semilocalized Excitons. *Phys. Rev. B* **8**, 2387 (1973).
24. Shah, J. *Ultrafast Spectroscopy of Semiconductors and Semiconductor Nanostructures*, (Springer, New York, 1999).
25. Chuang, C.-H. & Burda, C. Contribution of Femtosecond Laser Spectroscopy to the Development of Advanced Optoelectronic Nanomaterials. *J. Phys. Chem. Lett.* **3**, 1921–1927 (2012).
26. Gu, Q. L. *et al.* Deep level defects in a nitrogen-implanted ZnO homogeneous p-n junction. *Appl. Phys. Lett.* **92**, 222109 (2008).

Author contributions

E.L. and S.J. designed this work. E.L. and S.J. prepared the manuscript. E.L. performed TEM analysis. A.B. performed XPS study. T.S. performed femtosecond laser absorption spectroscopy. H.L. and D.-S.K. performed other materials analysis. T.S.K., K.S.S., M.R. and S.J. performed device fabrication and electrical analysis. G.-S.P. supervised this work. All authors discussed the results and implications and commented on the manuscript at all stages.

Additional information

Supplementary information accompanies this paper at <http://www.nature.com/scientificreports>

Competing financial interests: The authors declare no competing financial interests.

How to cite this article: Lee, E. *et al.* Nanocrystalline ZnON; High mobility and low band gap semiconductor material for high performance switch transistor and image sensor application. *Sci. Rep.* **4**, 4948; DOI:10.1038/srep04948 (2014).



This work is licensed under a Creative Commons Attribution-NonCommercial-NoDerivs 3.0 Unported License. The images in this article are included in the article's Creative Commons license, unless indicated otherwise in the image credit; if the image is not included under the Creative Commons license, users will need to obtain permission from the license holder in order to reproduce the image. To view a copy of this license, visit <http://creativecommons.org/licenses/by-nc-nd/3.0/>